

# CrystEngComm

Accepted Manuscript



This is an *Accepted Manuscript*, which has been through the Royal Society of Chemistry peer review process and has been accepted for publication.

*Accepted Manuscripts* are published online shortly after acceptance, before technical editing, formatting and proof reading. Using this free service, authors can make their results available to the community, in citable form, before we publish the edited article. We will replace this *Accepted Manuscript* with the edited and formatted *Advance Article* as soon as it is available.

You can find more information about *Accepted Manuscripts* in the [Information for Authors](#).

Please note that technical editing may introduce minor changes to the text and/or graphics, which may alter content. The journal's standard [Terms & Conditions](#) and the [Ethical guidelines](#) still apply. In no event shall the Royal Society of Chemistry be held responsible for any errors or omissions in this *Accepted Manuscript* or any consequences arising from the use of any information it contains.

**Influence of molecular structure of dithiolate ligands on  
crystal packing modes and magnetic properties in salts  
(Bz-Et<sub>3</sub>N)[Ni(dmit)<sub>x</sub>(mnt)<sub>2-x</sub>] (x = 0–2)**

Xuan-Rong Chen,<sup>a</sup> Yun-Xia Sui,<sup>\*b</sup> Lu Zhai<sup>a</sup>, Wei-Hua Ning,<sup>a</sup> Xiao-Ming Ren<sup>\*a, c, d</sup>

<sup>a</sup> State Key Laboratory of Materials-Oriented Chemical Engineering and College of Science, Nanjing University of Technology, Nanjing 210009, P. R. China

<sup>b</sup> Centre of Modern Analysis, Nanjing University, Nanjing 210093, P. R. China

<sup>c</sup> College of Materials Science and Engineering, Nanjing University of Technology, Nanjing 210009, P. R. China

<sup>d</sup> State Key Laboratory & Coordination Chemistry Institute, Nanjing University, Nanjing 210093, P. R. China

Tel.: +86 25 58139476

Fax: +86 25 58139481

E-mail: [suiyx@163.com](mailto:suiyx@163.com) (YXS); [xmren@njtech.edu.cn](mailto:xmren@njtech.edu.cn) (XMR)

## Abstract

Nickel-bis-dithiolene salts,  $(\text{Bz-Et}_3\text{N})[\text{Ni}(\text{dmit})_x(\text{mnt})_{2-x}]$  ( $x = 0-2$  for **1-3** and  $\text{mnt}^{2-} = \text{maleonitriledithiolate}$ ,  $\text{dmit}^{2-} = 2\text{-thioxo-1,3-dithiole-4,5-dithiolate}$ ), have been prepared and characterized. These three salts exhibit distinct anion packing structures and magnetic properties.  $[\text{Ni}(\text{mnt})_2]^-$  anions, in which the  $\text{mnt}^{2-}$  ligand has a reduced number of sulfur atoms, form one-dimensional anion stacks in **1**. Conversely,  $[\text{Ni}(\text{dmit})_2]^-$  anions, in which the  $\text{dmit}^{2-}$  ligand contains extended SR groups, give rise to a layered structure in **2**; the anion layer is comprised of co-facial  $[\text{Ni}(\text{dmit})_2]^-$  dimers, which are interconnected through short lateral-to-lateral  $\text{S}\cdots\text{S}$  and head-to-tail  $\text{S}\cdots\text{S}$  contacts. The heteroleptic  $[\text{Ni}(\text{dmit})(\text{mnt})]^-$  anions show one-dimensional anion stacking in **3**. Charge-assisted H-bonds are formed between the CN groups of the  $\text{mnt}^{2-}$  ligands and the H atoms of the cations in **1** and **3**; and between the terminal S atoms of the  $\text{dmit}^{2-}$  ligands and the H atoms of the cations in **2**. Both **1** and **3** show antiferromagnetic chain behavior. Within the respective magnetic chains, there are much stronger antiferromagnetic interactions in **3** than in **1**, and salt **2** shows antiferromagnetic dimer behavior.

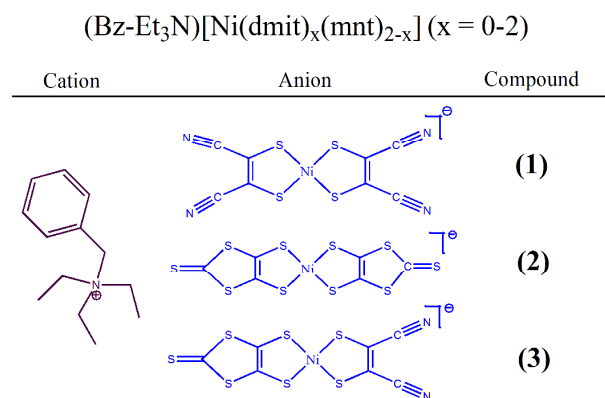
**Keywords:** metal-dithiolate salt, homoleptic and heteroleptic, diamagnetic  $\pi$ -dimer, spin gap

## 1. Introduction

Salts of planar metal-bis-1,2-dithiolenes (abbreviated as  $[M(\text{dithiolato})_2]^-$ ;  $M = \text{Ni}$ ,  $\text{Pd}$ , or  $\text{Pt}$ ) with organic or inorganic counter ions have been widely studied for many years due to their novel magnetic nature<sup>1-9</sup> and conductivity.<sup>10-19</sup> The electronic and magnetic properties of  $[M(\text{dithiolato})_2]^-$  salts strongly depend on the anion arrangements in their crystals since electronic and magnetic interactions between  $[M(\text{dithiolato})_2]^-$  anions may be realized through nonbonding interatomic contacts.

The arrangement of  $[M(\text{dithiolato})_2]^-$  anions in the crystal is strongly affected by the nature of the counterion, such as its size and shape<sup>20</sup>, and the electronic structure of the metal ion.<sup>21</sup> Moreover, the molecular structure of the dithiolate ligand is also an important factor.

To date, magnetic and conducting properties have been widely reported for homoleptic  $[M(\text{dithiolato})_2]^-$  salts, whereas these properties have been rarely investigated for heteroleptic metal-bis-1,2-dithiolene derivatives.<sup>22,23</sup> In this study, we have prepared and characterized three nickel-bis-dithiolene salts  $(\text{Bz-Et}_3\text{N})[\text{Ni}(\text{dmit})_x(\text{mnt})_{2-x}]$  (where  $x = 0-2$ ,  $\text{mnt}^{2-} = \text{maleonitriledithiolate}$ ,  $\text{dmit}^{2-} = 2\text{-thioxo-1,3-dithiole-4,5-dithiolate}$ ,  $\text{Bz-Et}_3\text{N}^+ = \text{tris(ethyl)benzylammonium}$ ; for the molecular structures, see [Scheme 1](#)), and have focused on investigating the influence of the molecular structure of the dithiolate on the crystal structures and magnetic properties of these salts.



**Scheme 1** Molecular structures of  $(\text{Bz-Et}_3\text{N})[\text{Ni}(\text{dmit})_x(\text{mnt})_{2-x}]$  ( $x = 0-2$ ).

## 2. Experimental

## 2.1. Chemicals and materials

The starting materials Na<sub>2</sub>mnt,<sup>24</sup> 4,5-bis(thiobenzoyl)-1,3-dithiol-2-thione,<sup>25</sup> and [Bz-Et<sub>3</sub>N]Cl<sup>26</sup> were synthesized according to the relevant literature procedures. [Bz-Et<sub>3</sub>N]<sub>2</sub>[Ni(mnt)<sub>2</sub>] was prepared according to a similar procedure as used for the preparation of [4'-NO<sub>2</sub>-BzPy]<sub>2</sub>[Ni(mnt)<sub>2</sub>] (where 4'-NO<sub>2</sub>-BzPy<sup>+</sup> = 4'-nitrobenzyl-1-pyridinium).<sup>27</sup>

## 2.2. Preparation

**Preparation of [Bz-Et<sub>3</sub>N][Ni(mnt)<sub>2</sub>] (1):** A solution of I<sub>2</sub> (205 mg, 0.80 mmol) in MeOH (10 mL) was slowly added to a solution of [Bz-Et<sub>3</sub>N]<sub>2</sub>[Ni(mnt)<sub>2</sub>] (724 mg, 1.0 mmol) in MeCN (25 mL), the mixture was stirred for 25 min, and then allowed to stand overnight. The dark powder formed was collected by filtration, washed with MeOH, and dried in vacuum. Yield ca. 71% (based on [Bz-Et<sub>3</sub>N]<sub>2</sub>[Ni(mnt)<sub>2</sub>]). Elemental analysis calcd. (%) for C<sub>21</sub>H<sub>22</sub>N<sub>5</sub>NiS<sub>4</sub>: C 47.47, H 4.17, N 13.18; found: C 47.38, H 4.34, N 12.35.

**Preparation of [Bz-Et<sub>3</sub>N][Ni(dmit)<sub>2</sub>] (2):** Sodium (92 mg, 4.0 mmol) was added to a suspension of 4,5-bis(thiobenzoyl)-1,3-dithiol-2-thione (812 mg, 2.0 mmol) in dry methanol (20 mL) under a nitrogen atmosphere at ambient temperature. After all of the sodium had been consumed, NiCl<sub>2</sub>·6H<sub>2</sub>O (238 mg, 1 mmol) was added and the mixture was vigorously stirred for 20 min. Solutions of I<sub>2</sub> (127 mg, 0.5 mmol) and [Bz-Et<sub>3</sub>N]Cl (228 mg, 1 mmol) in methanol were then added sequentially; the dark-blue powder precipitated was collected by filtration. Yield ca. 68% (based on NiCl<sub>2</sub>·6H<sub>2</sub>O). Elemental analysis calcd. (%) for C<sub>19</sub>H<sub>22</sub>NNiS<sub>10</sub>: C 35.45, H 3.44, N 2.18; found: C 35.31, H 3.71, N 1.83.

**Preparation of [Bz-Et<sub>3</sub>N][Ni(dmit)(mnt)] (3):** Complex **3** was obtained by ligand-exchange reaction between [Bz-Et<sub>3</sub>N][Ni(mnt)<sub>2</sub>] (159 mg, 0.3 mmol) and [Bz-Et<sub>3</sub>N][Ni(dmit)<sub>2</sub>] (193 mg, 0.3 mmol) in refluxing acetone (100 mL) under vigorous stirring over two days. The mixture was filtered and the filtrate was concentrated under reduced pressure overnight, whereupon micro-crystals were formed. Yield ca. 69%. Elemental analysis calcd. (%) for C<sub>20</sub>H<sub>22</sub>N<sub>3</sub>NiS<sub>7</sub>: C 40.88, H 3.77, N 7.15; found: C 40.76, H 3.78, N 7.25.

Crystals of **1–3** suitable for single-crystal X-ray diffraction analysis were obtained by slow evaporation of the solvents from saturated solutions of the respective compounds in acetonitrile or acetone at ambient temperature for 5–7 days.

### 2.3. Physical measurements

Elemental analyses of C, H, and N were performed with an Elementar Vario EL III analytical instrument. Powder X-ray diffraction (PXRD) data were collected on a Bruker D8 diffractometer with Cu- $K_{\alpha}$  radiation ( $\lambda = 1.5418 \text{ \AA}$ ). FTIR spectra were recorded on an IF66V FTIR (4000–400  $\text{cm}^{-1}$ ) spectrophotometer from samples in KBr pellets. Differential scanning calorimetry (DSC) was carried out on a Pyris 1 power-compensation differential scanning calorimeter in the range 98–298 K (from –175 to 25  $^{\circ}\text{C}$ ) for **1**, with a warming/cooling rate of 10  $\text{K}\cdot\text{min}^{-1}$  during the thermal cycles. Magnetic susceptibilities were measured on a Quantum Design MPMS-5 superconducting quantum interference device (SQUID) magnetometer over the temperature range 1.8–400 K.

### 2.4. Details of DFT calculations

All density functional theory (DFT) calculations were carried out utilizing the Gaussian-09 program.<sup>28</sup> Unrestricted geometry optimization for  $[\text{Ni}(\text{dmit})_x(\text{mnt})_{2-x}]^{-}$  ( $x = 0\text{--}2$ ) was performed using the hybrid functional UB3LYP with the LANL2DZ<sup>29–32</sup> basis set.

### 2.5. X-ray crystallography

Single-crystal X-ray diffraction data were collected for **1–3** at 293 K using graphite-monochromated Mo- $K_{\alpha}$  radiation ( $\lambda = 0.71073 \text{ \AA}$ ) on a CCD area detector (Bruker SMART). Data reductions and absorption corrections were performed with the SAINT and SADABS software packages,<sup>33</sup> respectively. Structures were solved by direct methods using the SHELXL-97 software package.<sup>34</sup> Non-hydrogen atoms were refined anisotropically using the full-matrix least-squares method on  $F^2$ . All hydrogen atoms were placed in calculated positions and refined as riding on the parent atoms. Details of the data collection, structure refinement, and crystallography are summarized in [Table 1](#).

**Table 1** Crystal data and structural refinement of **1–3**.

Compound	<b>1</b>	<b>2</b>	<b>3</b>
Temperature/K	293(2)	293(2)	293(2)
Chemical formula	C <sub>21</sub> H <sub>22</sub> N <sub>5</sub> NiS <sub>4</sub>	C <sub>19</sub> H <sub>22</sub> NNiS <sub>10</sub>	C <sub>20</sub> H <sub>22</sub> N <sub>3</sub> NiS <sub>7</sub>
Formula weight	531.41	643.69	587.59
Wavelength (Å)	0.71073	0.71073	0.71073
CCDC number	1003770	1003771	1003772
Crystal system	triclinic	triclinic	orthorhombic
Space group	<i>P</i> $\bar{1}$	<i>P</i> $\bar{1}$	<i>P</i> 2 <sub>1</sub> 2 <sub>1</sub>
<i>a</i> (Å)	11.9751(16)	9.6795(9)	7.9725(10)
<i>b</i> (Å)	13.956(2)	11.1962(11)	14.7293(17)
<i>c</i> (Å)	16.948(2)	12.7101(13)	44.097(5)
$\alpha$ (°)	103.541(4)	85.342(3)	90
$\beta$ (°)	106.768(4)	74.876(3)	90
$\gamma$ (°)	105.443(4)	85.864(3)	90
<i>V</i> (Å <sup>3</sup> )/ <i>Z</i>	2461.2(6)/4	1323.5(2)/2	5178.3(11)/8
Density (g·cm <sup>-3</sup> )	1.434	1.615	1.507
Abs. coeff. (mm <sup>-1</sup> )	1.146	1.533	1.328
<i>F</i> (000)	1100.0	662	2424
Data collection $\theta$ range	1.33–27.55	1.66–27.61	1.96–27.48
Index ranges	$-15 \leq h \leq 15$ , $-18 \leq k \leq 17$ , $-20 \leq l \leq 22$	$-12 \leq h \leq 12$ , $-14 \leq k \leq 14$ , $-16 \leq l \leq 16$	$-10 \leq h \leq 10$ , $-19 \leq k \leq 18$ , $-56 \leq l \leq 53$
Reflns. collected	34176	28116	78307
Independent reflns.	11087	6126	11801
Data/restraints/parameters	11087/0/565	6126/0/283	11801/0/566
Refinement method		least-squares refinement on <i>F</i> <sup>2</sup>	
Goodness-of-fit on <i>F</i> <sup>2</sup>	0.991	1.037	0.969
Final <i>R</i> indices [ <i>I</i> > 2 $\sigma$ ( <i>I</i> )]	<i>R</i> <sub>1</sub> = 0.0999 <i>wR</i> <sub>2</sub> = 0.2502	<i>R</i> <sub>1</sub> = 0.0340 <i>wR</i> <sub>2</sub> = 0.0786	<i>R</i> <sub>1</sub> = 0.0613 <i>wR</i> <sub>2</sub> = 0.0683
<i>R</i> indices (all data)	<i>R</i> <sub>1</sub> = 0.1988 <i>wR</i> <sub>2</sub> = 0.3107	<i>R</i> <sub>1</sub> = 0.0454 <i>wR</i> <sub>2</sub> = 0.0853	<i>R</i> <sub>1</sub> = 0.2155 <i>wR</i> <sub>2</sub> = 0.0893

$$R_1 = \frac{\sum(|F_o| - |F_c|)}{\sum|F_o|}, wR_2 = \frac{\sum w(|F_o|^2 - |F_c|^2)^2}{\sum w(|F_o|^2)^2}^{1/2}.$$

### 3. Results and discussion

#### 3.1. IR spectra

The IR spectra of **1–3** are displayed in [Figure 1](#) and the characteristic vibration bands together with their assignments are summarized in [Table 2](#). In the IR spectrum of **1**, an intense absorption band corresponding to the stretching vibration of C≡N in the mnt<sup>2-</sup> ligand is seen at 2206 cm<sup>-1</sup>, and the stretching vibration of C=C in the mnt<sup>2-</sup> ligand is seen at 1457 cm<sup>-1</sup>. In the IR spectrum of **2**, the characteristic bands ascribed to the stretching vibrations of C=C and C=S in the dmit<sup>2-</sup> ligand appear at 1346 and 1049 cm<sup>-1</sup>, respectively. In the IR spectrum of **3**, the vibration bands of C≡N in the mnt<sup>2-</sup> ligand as well as C=C and C=S in the dmit<sup>2-</sup> ligand appear at ca. 2201 cm<sup>-1</sup> and at 1319 and 1061 cm<sup>-1</sup>. It is noticeable that in the IR spectrum of the heteroleptic complex

**3**, the stretching vibrations of C≡N in the  $\text{mnt}^{2-}$  ligand and of C=C in the  $\text{dmit}^{2-}$  ligand are shifted to lower frequency, whereas the stretching vibration of C=S in the  $\text{dmit}^{2-}$  ligand is shifted to higher frequency with respect to those in the IR spectra of the homoleptic complexes **1** and **2** (see Figure 2).

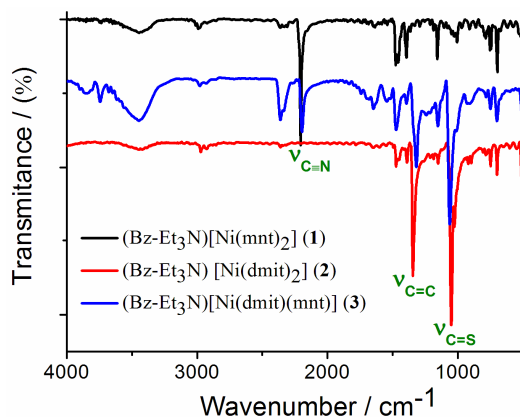


**Figure 1** Comparison of infrared spectra in the 4000–500  $\text{cm}^{-1}$  region for **1–3**.

**Table 2** Characteristic IR vibration bands ( $\text{cm}^{-1}$ ) and assignments in **1–3**.

<b>1</b>	<b>2</b>	<b>3</b>	Assignment
2992s	2972s	2978m	$\nu_{\text{C-H}}$ (alkyl chain)
2854m	2853m	2854m	
3093w, 3066w	3059w	3062w	$\nu_{\text{Ar-H}}$ , $\nu_{\text{Py-H}}$
3011w	3027w	3032w	
2206s	–	2195s	$\nu_{\text{C}\equiv\text{N}}$ ( $\text{mnt}^{2-}$ )
–	1346s	1319m	$\nu_{\text{C}=\text{C}}$ ( $\text{dmit}^{2-}$ )
1457m	–	1472m	$\nu_{\text{C}=\text{C}}$ ( $\text{mnt}^{2-}$ )
–	1049s	1061s	$\nu_{\text{C}=\text{S}}$

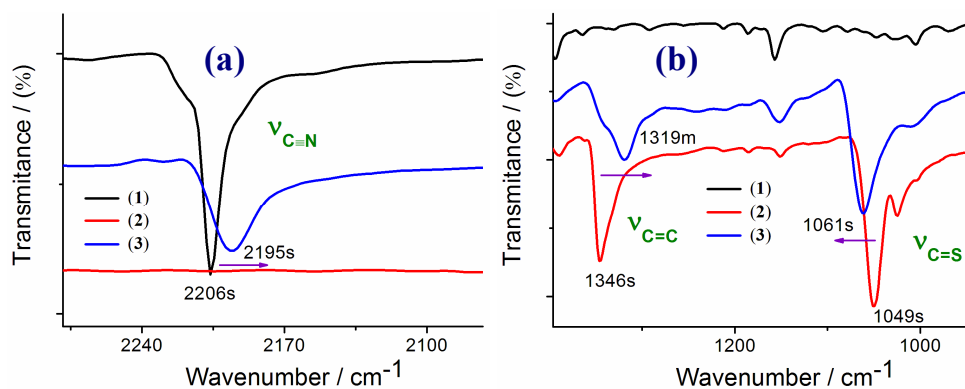


**Figure 2** (a) Stretching vibrations of the C≡N bonds of the  $\text{mnt}^{2-}$  ligands in **1** and **3**; (b) stretching vibrations of the C=C bonds and the C=S bonds in the  $\text{dmit}^{2-}$  ligands in **2** and **3**.

**Figure 3** shows the Kohn–Sham-type HOMOs of **1–3**, which indicate that the highest occupied molecular orbitals (HOMOs) of the monoanions  $[\text{Ni}(\text{dmit})_x(\text{mnt})_{2-x}]^-$  mostly consist of the  $\pi$  orbitals of the ligands admixed with a small amount of the 3d orbitals of Ni. The HOMOs are bonding with respect to the  $\pi(\text{C}=\text{C})$  and  $\pi(\text{C}\equiv\text{N})$  bonds, but antibonding with respect to the  $\sigma(\text{C}-\text{CN})$ ,  $\sigma(\text{C}-\text{S})$ , and  $\sigma(\text{Ni}-\text{S})$  bonds in the  $[\text{Ni}(\text{mnt})_2]^-$  anion. Likewise, the HOMOs are bonding with respect to the  $\pi(\text{C}=\text{C})$  bond and antibonding with respect to the  $\pi(\text{C}=\text{S})$ ,  $\sigma(\text{C}-\text{S})$ , and  $\sigma(\text{Ni}-\text{S})$  bonds in the  $[\text{Ni}(\text{dmit})_2]^-$  anion. The bonding features of  $\pi(\text{C}=\text{C})$ ,  $\pi(\text{C}=\text{S})$ ,  $\sigma(\text{C}-\text{S})$ , and  $\sigma(\text{Ni}-\text{S})$  are similar to those in the homoleptic  $[\text{Ni}(\text{mnt})_2]^-$  and  $[\text{Ni}(\text{dmit})_2]^-$ , whereas  $\pi(\text{C}\equiv\text{N})$  is nonbonding in nature in the heteroleptic  $[\text{Ni}(\text{dmit})(\text{mnt})]^-$ , making it weaker than in homoleptic  $[\text{Ni}(\text{mnt})_2]^-$ . As a result, the stretching vibration of the  $\text{C}\equiv\text{N}$  bond in the  $\text{mnt}^{2-}$  ligand is shifted towards lower frequency in the IR spectrum of heteroleptic  $[\text{Ni}(\text{dmit})(\text{mnt})]^-$ . In addition, the strong electron-attracting ability of the  $\text{mnt}^{2-}$  ligand with respect to the  $\text{dmit}^{2-}$  ligand leads to strengthening of the  $\pi(\text{C}=\text{S})$  and weakening of the  $\pi(\text{C}=\text{C})$  bonds in the  $\text{dmit}^{2-}$  moiety in the heteroleptic  $[\text{Ni}(\text{dmit})(\text{mnt})]^-$ , causing the  $\nu_{\text{C}=\text{C}}$  of the  $\text{dmit}^{2-}$  ligand to shift to lower frequency, whereas the  $\nu_{\text{C}=\text{S}}$  stretching vibration of the  $\text{dmit}^{2-}$  ligand is shifted to higher frequency in the IR spectrum of the heteroleptic complex **3** with respect to those in the IR spectra of the homoleptic complexes **1** and **2**.

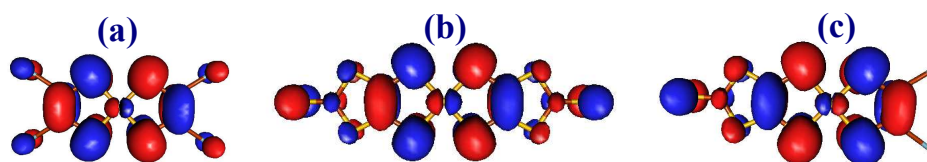


**Figure 3** HOMOs of (a)  $[\text{Ni}(\text{mnt})_2]^-$ , (b)  $[\text{Ni}(\text{dmit})_2]^-$ , and (c)  $[\text{Ni}(\text{dmit})(\text{mnt})]^-$  obtained from DFT calculations at the B3LYP/LANL2DZ level of theory.

### 3.2. Crystal structures

Compound **1** crystallizes in the triclinic space group  $P\bar{1}$ . As displayed in **Figure 4a**, the asymmetric unit consists of two pairs of  $\text{Bz-Et}_3\text{N}^+$  cations and  $[\text{Ni}(\text{mnt})_2]^-$  anions. Two different cations exhibit distinct conformations and their phenyl rings form a dihedral angle of  $70.4^\circ$ . The bond lengths and angles in the two different cations fall within the expected ranges. The two crystallographically inequivalent anions show the same orientation and the mean molecule planes defined by four-coordinate S atoms

form a dihedral angle of  $2.3^\circ$ . The bond lengths and angles in the planar  $[\text{Ni}(\text{mnt})_2]^-$  motifs, listed in Table S1, are normal and comparable to those in reported  $[\text{Ni}(\text{mnt})_2]^-$  compounds.<sup>27</sup>

The anions are aligned into columnar stacks along the *b*-axis direction and the cations occupy the space between the anionic stacks in **1**, as shown in Figure 4b. The anion stack is formed in the transverse offset mode between the adjacent anions and the anions with Ni1 and Ni2 are aligned in the manner of ...Ni2/Ni1/Ni1/Ni2/Ni2... to give three different adjacent Ni...Ni distances ( $d_{\text{Ni2-Ni1}} = 3.636(2) \text{ \AA}$ ,  $d_{\text{Ni1-Ni1}} = 4.058(2) \text{ \AA}$ ,  $d_{\text{Ni2-Ni2}} = 3.816(2) \text{ \AA}$ ). The typical interatomic distances within an anion stack are summarized in Table 3.

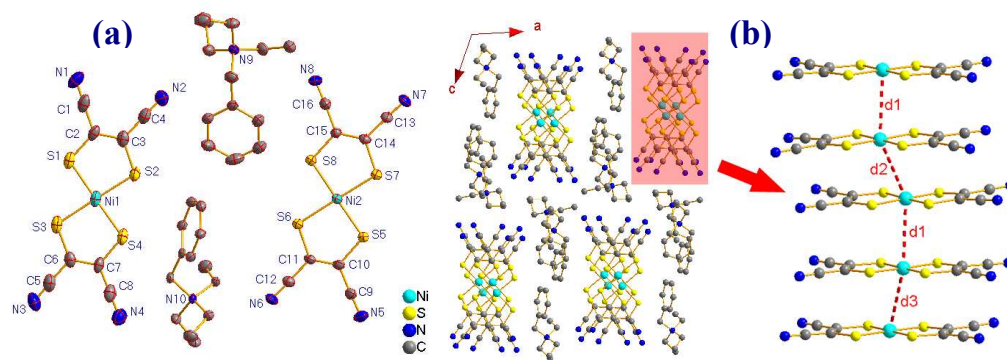


**Figure 4** (a) Molecular structure of **1** with displacement ellipsoids at the 20% probability level (hydrogen atoms omitted for clarity); (b) packing diagram showing segregated columnar stacks of anions viewed along the *b*-axis; the stack of anions displays non-equivalent distances in **1**.

As shown in Figure 5, there are charge-assisted H-bond interactions between the H atoms of the alkyl groups in the cations and the N atoms of the CN groups in the anions, whereby the contact between H and N is less than the sum of their van der Waals radii ( $2.8 \text{ \AA}$ ).<sup>35</sup> The H-bond parameters are summarized in Table 3.

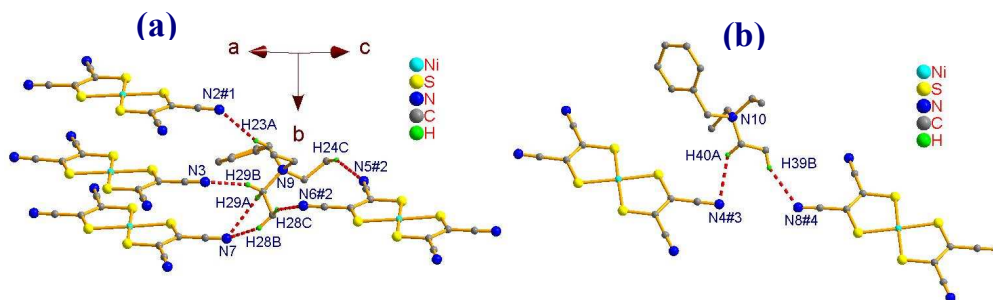


**Figure 5** (a, b) Charge-assisted H-bonds between H atoms in the cations and N atoms of CN groups in the anions (with the symmetry codes: #1 =  $1-x, 1-y, -z$ ; #2 =  $x, y, 1+z$ ; #3 =  $-1+x, -1+y, z$ ; #4 =  $1-x, 1-y, 1-z$ ).

Wang and coworkers have previously published the crystal structure of **2**.<sup>36</sup> For comparison, we describe its structure here. The crystal of **2** belongs to the triclinic space group  $P-1$ , the asymmetric unit contains one pair of a Bz-Et<sub>3</sub>N<sup>+</sup> cation and an [Ni(dmit)<sub>2</sub>]<sup>-</sup> anion (Figure 6a). The bond lengths and angles in the cation are comparable to those in **1** and in agreement with the values reported in the literature.<sup>36</sup> The typical bond lengths and angles in the [Ni(dmit)<sub>2</sub>]<sup>-</sup> anion fall within the expected ranges and are summarized in Table S1.

The anions and cations form an alternating layer arrangement, as shown in Figure 6b, and the molecular layers are parallel to the (0 -1 1) crystallographic plane. The cations show the same molecular orientation along the  $a$ -axis, while the neighboring cations display the opposite orientation along the  $b+c$  direction of a cation layer (see Figure 6c); there are only van der Waals forces between the adjacent cations in a cation layer. The anionic layer is constructed from  $\pi$ -type anion dimers, in which two anions are related to each other through an inversion center and stacked in transverse and longitudinal offset modes. The [Ni(dmit)<sub>2</sub>]<sup>-</sup> anions between the neighboring dimers connect in two fashions, that is, through lateral S $\cdots$ S contacts along the  $a$ -axis and head-to-tail S $\cdots$ S contacts along the  $b+c$  direction. The shorter interatomic distances, which are less than the sum of the van der Waals radii of two S atoms (3.7 Å)<sup>35</sup> in an anion layer, are illustrated in Figure 6d and summarized in Table 3. As displayed in Figure 6e, charge-assisted H-bonds are formed between the cations and anions, with the distances  $d_{\text{Ni}1\cdots\text{H}13\text{A}} = 2.830$  and  $d_{\text{H}19\text{B}\cdots\text{S}6\#5} = 2.826$  Å and the symmetry code #5 =  $2-x, 1-y, 1-z$ , and these interatomic separations are less than

the sum of the van der Waals radii of an H atom and Ni (S).<sup>35</sup>

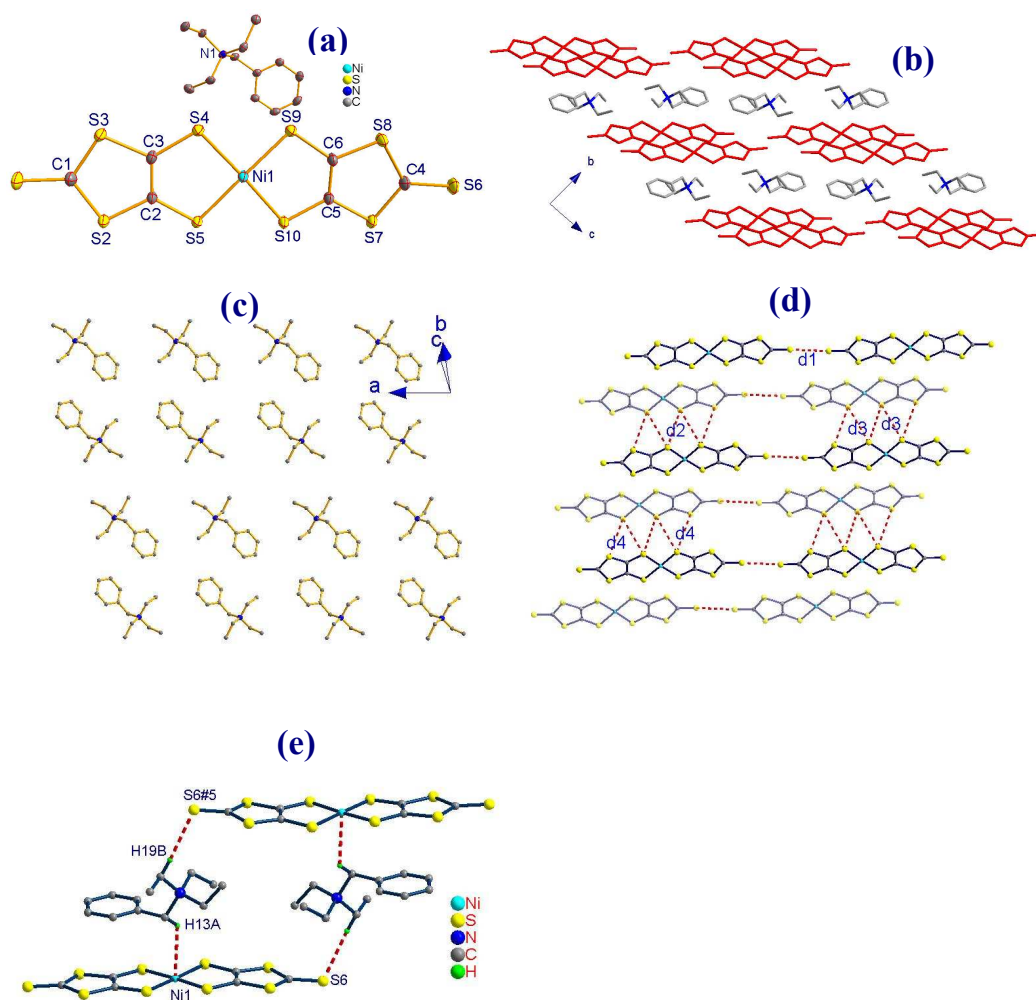


**Figure 6** (a) ORTEP view of **2** with displacement ellipsoids at the 20% probability level (hydrogen atoms omitted for clarity), (b) alternating layers of Bz-Et<sub>3</sub>N<sup>+</sup> cations and [Ni(dmit)<sub>2</sub>]<sup>−</sup> anions viewed along the *a*-axis in **2**, (c) cation layer, (d) anion layer, where the dotted lines represent S⋯S contacts < 3.7 Å,<sup>35</sup> and (e) charge-assisted H-bonds between cations and anions.

Complex **3** crystallizes in the orthorhombic space group  $P2_12_12_1$ , which is a non-centrosymmetric space group; refinement gave a Flack parameter of 0.009(13). As displayed in **Figure 7a**, the asymmetric unit is comprised of two pairs of [Ni(dmit)(mnt)]<sup>−</sup> anions and Bz-Et<sub>3</sub>N<sup>+</sup> cations. The bond distances and angles in the Bz-Et<sub>3</sub>N<sup>+</sup> motif are analogous to the values in **1** and **2**. The [Ni(dmit)(mnt)]<sup>−</sup> anion

adopts a planar geometry, with dihedral angles of  $2.9^\circ$  for the Ni1 anion and  $2.4^\circ$  for the Ni2 anion between the mean molecule planes of the  $\text{dmit}^{2-}$  and  $\text{mnt}^{2-}$  moieties. The Ni–S bond distances range from 2.145(1) to 2.178(2) Å for the Ni1 anion and from 2.139(1) to 2.170(2) Å for the Ni2 anion; the S–Ni–S bite angles are  $92.88(5)^\circ$  and  $92.56(6)^\circ$  for the Ni1 anion and  $92.57(5)^\circ$  and  $92.82(5)^\circ$  for the Ni2 anion; these values are in good agreement with those in  $[\text{BzQI}][\text{Ni}(\text{dmit})(\text{mnt})]$  ( $\text{BzQI}^+ = 1\text{-}(\text{benzyl})\text{quinolinium}$ ).<sup>22</sup>

As shown in **Figure 7b**, the anions form columnar stacks along the *a*-axis and the cations occupy the space between these stacks; this situation is analogous to that in **1**. The heteroleptic anions adopt the same orientation within a stack and align in the manner of ...Ni1/Ni2/Ni1/Ni2... (**Figure 7c**) to give two types of stacking patterns: (1) two anions superimpose to give an eclipsed overlap (**Figure 7d**) with shorter Ni...Ni and S...S contacts (see **Table 3**) or (2) two anions stack in transverse and longitudinal offset modes (**Figure 7e**).

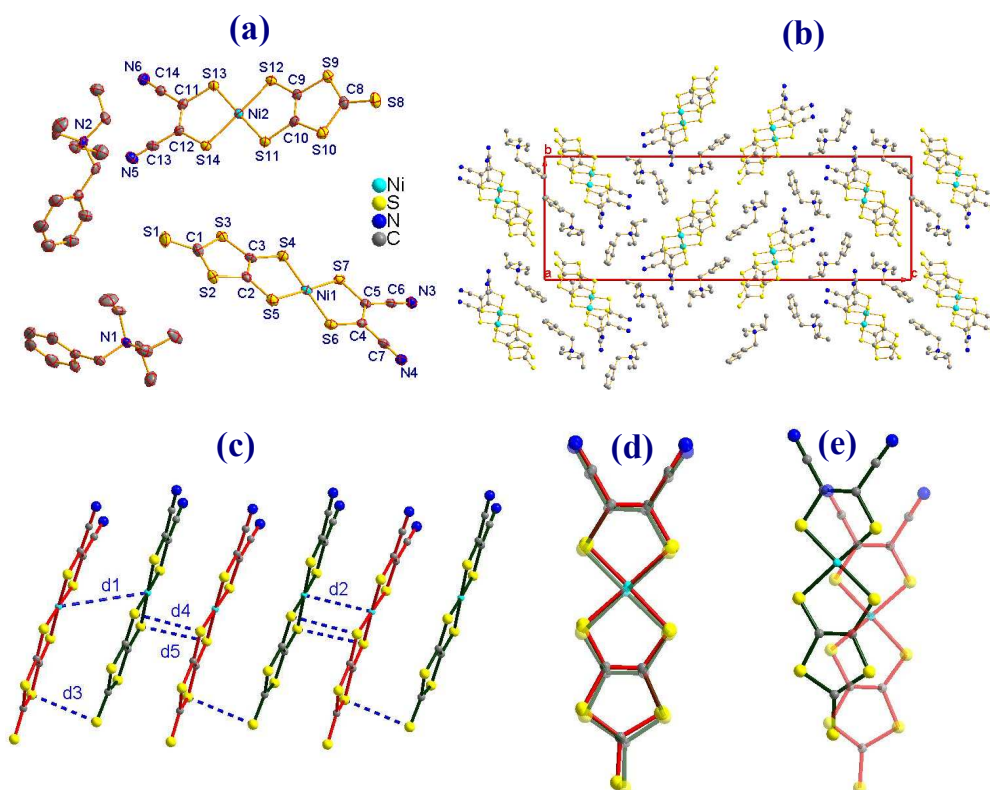


**Figure 7** (a) ORTEP view of **3** with displacement ellipsoids at the 20% probability level, (b) packing diagram showing segregated columnar stacks of anions viewed along

the *a*-axis, (c) columnar stack of anions where Ni1 and Ni2 anions are presented in different colors, and (d, e) top views of two stacking patterns within an anion column.

As displayed in **Figure 8**, short H···N contacts are observed between the cations and anions, indicating the existence of charge-assisted H-bonds, and the H-bond distances are listed in **Table 3**.

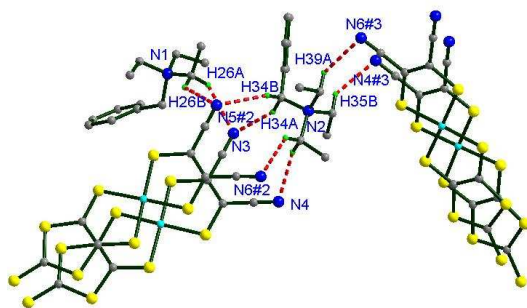


**Figure 8** Charge-assisted H-bonds between cations and anions in **3**.

**Table 3** Typical interatomic distances (Å) within an anion stack and a cation stack as well as between anion and cation stacks in **1–3**.

	<b>1</b>	<b>2</b>	<b>3</b>
<i>d</i> 1	3.636(2)	<i>d</i> 1	3.434(1)
<i>d</i> 2	4.058(2)	<i>d</i> 2	3.530(8)
<i>d</i> 3	3.816(2)	<i>d</i> 3	3.656(7)
<i>d</i> <sub>H23A...N2#1</sub>	2.599	<i>d</i> 4	3.605(9)
<i>d</i> <sub>H29B...N3</sub>	2.366	<i>d</i> <sub>H19B...S6#5</sub>	2.826
<i>d</i> <sub>H29A...N7</sub>	2.693	<i>d</i> <sub>Ni1...H13A</sub>	2.830
<i>d</i> <sub>H28B...N7</sub>	2.701		
<i>d</i> <sub>H28C...N6#2</sub>	2.693		
<i>d</i> <sub>H24C...N5#2</sub>	2.617		
<i>d</i> <sub>H40A...N4#3</sub>	2.680		
<i>d</i> <sub>H39B...N8#4</sub>	2.593		
			<i>d</i> <sub>H26A...N3</sub>
			<i>d</i> <sub>H26B...N5#2</sub>
			<i>d</i> <sub>H34B...N5#2</sub>
			<i>d</i> <sub>H34A...N3</sub>
			<i>d</i> <sub>H37A...N6#2</sub>
			<i>d</i> <sub>H37B...N4</sub>
			<i>d</i> <sub>H39A...N6#3</sub>
			<i>d</i> <sub>H35B...N4#3</sub>
			2.574
			2.741
			2.692
			2.408
			2.552
			2.549
			2.748
			2.511
#1 = 1-x, 1-y, -z; #2 = x, y, 1+z; #3 = -1+x, -1+y, z; #4 = 1-x, 1-y, 1-z.		#5 = 2-x, 1-y, 1-z.	#2 = 1+x, y, z
			#3 = 1-x, 0.5+y, 0.5-z.

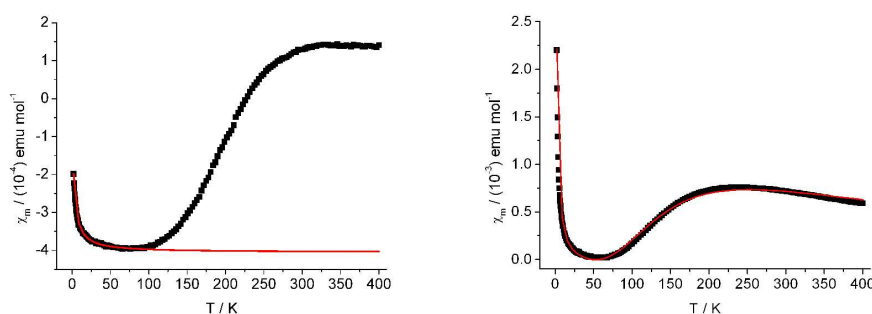
### 3.3. Influence of the dithiolene ligand on crystal structure

In crystals of **1–3**, a common feature is that the anions favor the formation of co-facial dimers or columnar stacks. This is due to the fact that the planarity and conjugation promote negative charge delocalization over the entire molecular skeleton

in the anion, thereby minimizing coulombic repulsions between co-facially stacked anions. The obvious influence of the dithiolate ligand on the packing structure is manifested as follows: (1) the anions in **1** and **3** form columnar stacks owing to the  $\text{mnt}^{2-}$  ligand with a reduced number of sulfur atoms preventing the formation of lateral-to-lateral S $\cdots$ S contacts between the neighboring  $[\text{Ni}(\text{mnt})_2]^-/[\text{Ni}(\text{dmit})(\text{mnt})]^-$  anions, while the layered arrangement in **2** is due to the  $\text{dmit}^{2-}$  ligand with extended SR groups favoring the formation of lateral-to-lateral and head-to-tail S $\cdots$ S contacts. (2) The N atom of the CN group has a lone pair of electrons, which is favorable for the formation of charge-assisted H-bonds between N and H atoms with a partial positive charge, and such types of H-bonds are observed in **1** and **3**. Charge-assisted H-bonds are formed between the terminal S atoms of the  $\text{dmit}^{2-}$  ligands and the H atoms in the alkyl groups of **2**.

### 3.4. Magnetic properties

The temperature-dependent experimental magnetic susceptibilities of **1–3** in the temperature range 1.8–400 K are displayed in **Figure 9a–c**, respectively, where  $\chi_m$  represents the molar magnetic susceptibility corresponding to one  $[\text{Ni}(\text{dmit})_x(\text{mnt})_{2-x}]^-$  per formula unit and no diamagnetic correction was made. The three compounds show Curie–Weiss-type paramagnetic character in the low-temperature regions (approximately below 75 K for **1**, 60 K for **2**, and 200 K for **3**, respectively). This type of paramagnetism, so-called magnetic impurity, is due to uncoupled spins arising from lattice defects.



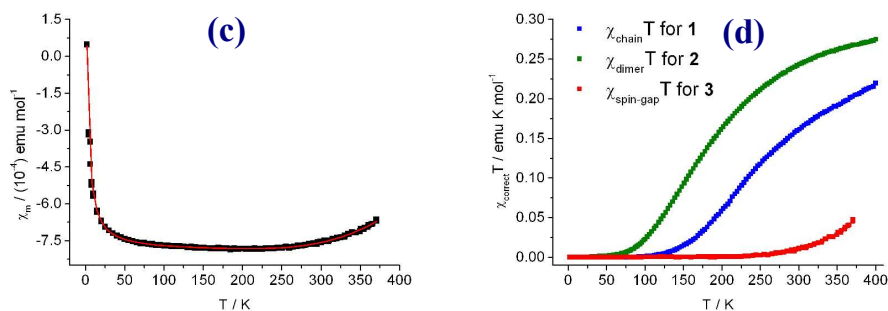


**Figure 9** Magnetic susceptibility  $\chi_m$  as a function of temperature for (a) **1**, (b) **2**, and (c) **3**, where the solid squares represent experimental data and the red solid lines are derived from the fitted parameters; (d) plots of  $\chi_{\text{chain}}T$  versus  $T$  for **1**,  $\chi_{\text{dimer}}T$  versus  $T$  for **2**, and  $\chi_{\text{spin-gap}}T$  versus  $T$  for **3**.

The magnetic susceptibility of **1** shows an exponential drop when the temperature is roughly lower than 320 K, indicating the existence of a spin gap (the energy gap is defined as the energy difference between the magnetic ground state and the first excited state in the low-energy spectrum). Structural analysis indicated that the  $S = 1/2$   $[\text{Ni}(\text{mnt})_2]^-$  anions in the crystal of **1** form a 1-D irregular stack with three different neighboring Ni $\cdots$ Ni distances, implying the existence of three distinct magnetic exchange constants within an  $S = 1/2$   $[\text{Ni}(\text{mnt})_2]^-$  chain. It was not possible to fit the temperature dependence of the magnetic susceptibility data for a spin chain system with three magnetic exchange constants owing to the lack of an expression for magnetic susceptibility versus temperature. As a result, we used Equation (1) to estimate the magnetic impurity and temperature-independent magnetic susceptibility, which include contributions from core diamagnetism and possible van Vleck paramagnetism, by fitting the magnetic susceptibility data in the low-temperature region.

$$\chi_m = \frac{C}{T - \theta} + \chi_0 \quad (1)$$

In Equation (1), the term  $C/(T - \theta)$  represents the magnetic susceptibility arising from magnetic impurity and  $\chi_0$  denotes the temperature-independent magnetic susceptibility. The fit was performed for the magnetic susceptibility data of **1** in the range 1.8–76 K using Equation (1), to give the reasonable parameters  $C = 8.3(1) \times 10^{-4} \text{ emu K mol}^{-1}$ ,  $\theta = -1.99(8) \text{ K}$ , and  $\chi_0 = -4.1(1) \times 10^{-4} \text{ emu mol}^{-1}$ . Magnetic impurity from the

uncoupled  $[\text{Ni}(\text{mnt})_2]^-$  anions was estimated to be ca. 0.22%, based on the  $C$  value in **1**. To remove the magnetic impurity and temperature-independent paramagnetism terms from the experimental magnetic susceptibility ( $\chi_m$ ), the magnetic susceptibility arising from the magnetic chains ( $\chi_{\text{chain}}$ ) was obtained and the product of  $\chi_{\text{chain}}$  and  $T$  versus  $T$  was plotted, as shown in **Figure 9d**, which demonstrated the existence of antiferromagnetic interactions within an anion stack and a singlet ground state in **1**.

On the basis of the crystal structure analysis, there exist three different magnetic exchange pathways between the neighboring anions in an  $[\text{Ni}(\text{dmit})_2]^-$  layer, namely: (1) magnetic coupling between two monomers in a co-facial  $\pi$ -type dimer through orbital overlap or spin polarization; (2) two neighboring anions along the short molecule axis direction through lateral-to-lateral  $\text{S}\cdots\text{S}$  contacts; (3) two neighboring anions along the long molecular axis direction through head-to-tail  $\text{S}\cdots\text{S}$  contacts. Obviously, the magnetic coupling is much stronger through  $\pi$ -orbital overlap in the co-facial  $\pi$ -type dimer than in the other two cases. As a result, we used the magnetic exchange mode for a dimer to analyze the magnetic behavior of **2**. To further consider the contribution of magnetic impurity and temperature-independent paramagnetism, the experimental magnetic susceptibility is expressed as shown below:

$$\chi_m = \frac{Ng^2\mu_B^2}{k_B T} \cdot \frac{1}{3 + \exp(-2J/k_B T)} + \frac{C}{T - \theta} + \chi_0 \quad (2)$$

Where  $J$  is the magnetic exchange constant within the co-facial  $\pi$ -type dimer, and the first term in Equation (2) is based on the spin Hamiltonian  $\mathbf{H} = -2J\mathbf{S}_1\mathbf{S}_2$ ; other symbols in Equation (2) have their normal meanings. The best fit was obtained for the magnetic susceptibility data in the range 1.8–400 K, giving  $J/k_B = -204.8(0)$  K,  $g = 2.125(8)$ ,  $C = 4.8(3) \times 10^{-3}$  emu K mol $^{-1}$ ,  $\theta = -0.06(4)$  K, and  $\chi_0 = -1.1(1) \times 10^{-4}$  emu mol $^{-1}$ . Magnetic impurity from uncoupled  $[\text{Ni}(\text{dmit})_2]^-$  anions was estimated to be ca. 1.28%, based on the fitted  $C$  value in **2**. A plot of  $\chi_{\text{dimer}}T$  versus  $T$  is shown in **Figure 9d**, where  $\chi_{\text{dimer}}$  represents the magnetic susceptibility contributed from the dimers.

A plot of  $\chi_m T$  for **3** in the range 200–380 K shows the magnetic character of a spin-gap system. Crystal structure analysis indicated that the  $[\text{Ni}(\text{dmit})(\text{mnt})]^-$  anions form a strongly dimerized stack with two types of neighboring  $\text{Ni}\cdots\text{Ni}$  distances in **3**.

Equation (3), used to describe the magnetic behavior of a spin-gap system, was chosen to fit the temperature-dependent magnetic susceptibility of **3**.<sup>37, 38</sup>

$$\chi_m = \frac{\alpha}{T^{\gamma_0}} \exp\left(-\frac{\Delta}{k_B T}\right) + \frac{C}{T - \theta} + \chi_0 \quad (3)$$

In Equation (3), the parameter  $\alpha$  is a constant corresponding to the dispersion of excitation energy,  $\Delta/k_B$  is the magnitude of the spin gap,  $\gamma_0$  is a constant ( $\gamma_0 = 0.5$ ), and  $C$  and  $\chi_0$  have their normal meanings. The variable-temperature magnetic susceptibility data of **3** in the range 1.8–400 K were fitted to Equation (3), which yielded parameters of  $\alpha = 1.2(4)$ ,  $\Delta/k_B = 2323(16)$  K,  $C = 2.62(4) \times 10^{-3}$  emu·mol<sup>-1</sup>,  $\theta = -1.13(6)$  K, and  $\chi_0 = -8(0) \times 10^{-4}$  emu·mol<sup>-1</sup>. The large spin gap results in **3** being almost diamagnetic in the range 1.8–400 K. On the basis of the fitted  $C$  value for **3**, the magnetic impurity from the uncoupled [Ni(dmit)(mnt)]<sup>-</sup> anions was estimated to be ca. 0.7%. A plot of  $\chi_{\text{spin-gap}}$  versus  $T$  is displayed in Figure 9d, where  $\chi_{\text{spin-gap}}$  represents the magnetic susceptibility contributed from the spin-gap term.

#### 4. Conclusion

In summary, we have investigated the influence of the molecular structures of dithiolene ligands on the anion packing structures and magnetic properties of nickel-bis-dithiolene salts (Bz-Et<sub>3</sub>N)[Ni(dmit)<sub>x</sub>(mnt)<sub>2-x</sub>] ( $x = 0-2$ ). We have found that: (1) the [Ni(mnt)<sub>2</sub>]<sup>-</sup> anion, in which the mnt<sup>2-</sup> ligand has a reduced number of sulfur atoms, favors the formation of 1-D anion stacks; the [Ni(dmit)<sub>2</sub>]<sup>-</sup> anion, in which the dmit<sup>2-</sup> ligand contains extended SR groups, tends to form co-facial stacks through short lateral-to-lateral S··S and head-to-tail S··S contacts; the heteroleptic [Ni(dmit)(mnt)]<sup>-</sup> anion shows an analogous packing structure to that seen with the [Ni(mnt)<sub>2</sub>]<sup>-</sup> anion. (2) Charge-assisted H-bonds are formed between the CN groups of the mnt<sup>2-</sup> ligands and the H atoms of the cations in the nickel-bis-dithiolene salts with mnt<sup>2-</sup> ligands, and between the terminal S atoms of the dmit<sup>2-</sup> ligands and the H atoms of the cations in the nickel-bis-dithiolene salts with dmit<sup>2-</sup> ligands. (3) There are much stronger antiferromagnetic interactions in the co-facial  $\pi$ -type dimer of **3** than that of **1**, which is due to the existence of more extended electron structure in [Ni(dmit)(mnt)]<sup>-</sup> than that in [Ni(mnt)<sub>2</sub>]<sup>-</sup>, leading to more efficient orbital overlap between two monomers in **3**

compared to that in **1**.

### **Supporting material**

Crystallographic data in CIF format for **1–3**. The powder X-ray diffraction profiles in PDF format are available free of charge.

### **Acknowledgements**

The authors thank the Priority Academic Program Development of Jiangsu Higher Education Institutions and the National Natural Science Foundation of China (Grant nos. 91122011 and 21271103) for financial support.

## Notes and References

1. B. Zhang, Y. Zhang, D. B. Zhu, *Chem. Commun.*, **2012**, 197.
2. B. Zhang, Z. M. Wang, Y. Zhang, H. Kobayashi, M. Kurmoo, T. Mori, F. L. Pratt, K. Inoue, D. B. Zhu, *Polyhedron*, 2007, **26**, 1800.
3. H. L. Peng, C. B. Ran, Z. F. Liu, Y. Z. Long, Z. M. Wang, Z. Q. Yu, H. L. Sun, Y. G. Wei, S. Gao, Z. J. Chen, E. Q. Chen, *J. Phys. Chem. C*, 2008, **112**, 11001.
4. B. Zhou, H. Yajima, A. Kobayashi, Y. Okano, H. Tanaka, T. Kumashiro, E. Nishibori, H. Sawa, H. Kobayashi, *Inorg. Chem.*, 2010, **49**, 6740.
5. A. T. Coomber, D. Beljonne, R. H. Friend, J. L. Brédas, A. Charlton, N. Robertson, A. E. Underhill, M. Kurmoo, P. Day, *Nature*, 1996, **380**, 144.
6. O. Jeannin, R. Clérac, M. Fourmigué, *J. Am. Chem. Soc.*, 2006, **128**, 14649.
7. M. Fourmigué, *Acc. Chem. Res.*, 2004, **37**, 179.
8. R. D. Willett, C. J. Gómez-Garcí, B. L. Ramakrishna, B. Twamley, *Polyhedron*, 2005, **24**, 2232.
9. R. A. L. Silva, A. I. S. Neves, E. B. Lopes, I. C. Santos, J. T. Coutinho, L. C. J. Pereira, C. Rovira, M. Almeida, D. Belo, *Inorg. Chem.*, 2013, **52**, 5300.
10. T. Akutagawa, T. Hasegawa, T. Nakamura, T. Inabe, G. Saito, *Chem. Eur. J.*, 2002, **8**, 4402.
11. T. Akutagawa, S. Takeda, T. Hasegawa, T. Nakamura, *J. Am. Chem. Soc.*, 2004, **126**, 291.
12. H. Kobayashi, A. Kobayashi, H. Tajima, *Chem. Asian J.*, 2011, **6**, 1688.
13. B. Zhou, A. Kobayashi, Y. Okano, T. Nakashima, S. Aoyagi, E. Nishibori, M. Sakata, M. Tokumoto, H. Kobayashi, *Adv. Mater.*, 2009, **21**, 3596.
14. J. A. Schlueter, L. Wiehl, H. Park, M. de Souza, M. Lang, H. J. Koo, M. H. Whangbo, *J. Am. Chem. Soc.*, 2010, **132**, 16308.
15. C. Rovira, *Chem. Rev.*, 2004, **104**, 5289.
16. F. Wudl, D. Wobschall, E. J. Hufnagel, *J. Am. Chem. Soc.*, 1972, **94**, 670.
17. J. Ferraris, D. O. Cowan, V. Walatka, J. H. Perlstein, *J. Am. Chem. Soc.*, 1973, **95**, 948.
18. J. Lieffrig, O. Jeannin, T. Guizouarn, P. Auban-Senzier, M. Fourmigué, *Cryst. Grow. & Des.*, 2012, **12**, 4248.
19. T. Shirahata, K. Shiratori, S. Kumeta, T. Kawamoto, T. Ishikawa, S. Y. Koshihara, Y. Nakano, H. Yamochi, Y. Misaki, T. Mori, *J. Am. Chem. Soc.*, 2012, **134**, 13330.

20. H. B. Duan, X. M. Ren, Q. J. Meng, *Coord. Chem. Rev.* 2010, **254**, 1509.
21. W. B. Pei, J. S. Wu, X. M. Ren, Z. F. Tian, J. L. Xie, *Dalton Trans.*, 2012, **41**, 2667.
22. R. Kato, Y. Kashimura, H. Sawa, Y. Okano, *Chem. Lett.*, 1997, 921.
23. B. Cai, J. L. Liu, X. L. Sheng, X. M. Ren, *Inorg. Chem. Commun.*, 2011, **14**, 1971.
24. A. Davison, H. R. Holm, *Inorg. Synth.*, 1967, **10**, 8.
25. C. S. Wang, A. S. Batsanov, M. R. Bryce, J. A. K. Howard, *Synthesis*, **1998**, 1615.
26. S. B. Bulgarevich, D. V. Bern, D. Y. Movshovic, P. Finocchiaro, S. Failla, *J. Mol. Struct.*, 1994, **317**, 147.
27. X. M. Ren, Q. J. Meng, Y. Song, C. S. Lu, C. J. Hu, *Inorg. Chem.*, 2002, **41**, 5686.
28. M. J. Frisch, G. W. Trucks, H. B. Schlegel, et al., *Gaussian 09*, Revision **A.02**, Gaussian, Inc., Wallingford CT, 2009.
29. T. H. Dunning Jr., P. J. Hay, *Modern Theoretical Chemistry*, Plenum, New York, 1976, p. 1-28.
30. P. J. Hay, W. R. Wadt, *J. Chem. Phys.*, 1985, **82**, 270.
31. W. R. Wadt, P. J. Hay, *J. Chem. Phys.*, 1985, **82**, 284.
32. P. J. Hay, W. R. Wadt, *J. Chem. Phys.*, 1985, **82**, 299.
33. SMART and SAINT (Software Packages), Siemens Analytical X-ray Instruments Inc., Madison, WI, 1996.
34. G.M. Sheldrick, SHELX-97, Program for the Refinement of Crystal Structures, University of Göttingen, Germany, 1997.
35. A. Bondi, *J. Phys. Chem.*, 1964, **68**, 441.
36. X. Q. Wang, Q. Ren, H. L. Fan, J. W. Chen, Z. H. Sun, T. B. Li, X. T. Liu, G. H. Zhang, D. Xu, W. L. Liu, *J. Cryst. Growth.*, 2010, **312**, 2206.
37. D. C. Johnston, R. K. Kremer, M. Troyer, X. Wang, A. Klümper, S. L. Bud'ko, A. F. Panchula, P. C. Canfield, *Phys. Rev. B.*, 2000, **61**, 9558.
38. M. Troyer, H. Tsunetsugu, D. Wurtz, *Phys. Rev. B*, 1994, **50**, 13515.